Received: 8 December 2019 | Revised: 3 March 2020 | Accepted: 4 March 2020 | Uncorrected manuscript published on: 6 March 2020

DOI: 10.1111/tra.12727

TOOLBOX

Traffic WILEY

High-content imaging and structure-based predictions reveal functional differences between Niemann-Pick C1 variants

Lauri Vanharanta[1,2] | Johan Peränen[1,2] | Simon G. Pfisterer[1] | Giray Enkavi[3,4] | Ilpo Vattulainen[3,4] | Elina Ikonen[1,2]

[1]Department of Anatomy and Stem Cells and Metabolism Research Program, Faculty of Medicine, University of Helsinki, Helsinki, Finland

[2]Minerva Foundation Institute for Medical Research, Helsinki, Finland

[3]Department of Physics, University of Helsinki, Helsinki, Finland

[4]Computational Physics Laboratory, Tampere University of Technology, Tampere, Finland

Correspondence
Elina Ikonen, Department of Anatomy, Faculty of Medicine, Haartmaninkatu 8, Helsinki 00290, Finland.
Email: elina.ikonen@helsinki.fi

Funding information
Orion Research Foundation; HiLIFE; Sigrid Juselius Foundation; Academy of Finland, Grant/Award Numbers: 282192, 307415, 312491

Peer Review
The peer review history for this article is available at https://publons.com/publon/10.1111/tra.12727/.

Abstract

The human Niemann-Pick C1 (NPC1) gene encoding a 1278 amino acid protein is very heterogeneous. While some variants represent benign polymorphisms, NPC disease carriers and patients may possess rare variants, whose functional importance remains unknown. An NPC1 cDNA construct known as NPC1 wild-type variant (WT-V), distributed between laboratories and used as a WT control in several studies, also contains changes regarding specific amino acids compared to the NPC1 Genbank reference sequence. To improve the dissection of subtle functional differences, we generated human cells stably expressing NPC1 variants from the AAVS1 safe-harbor locus on an NPC1-null background engineered by CRISPR/Cas9 editing. We then employed high-content imaging with automated image analysis to quantitatively assess LDL-induced, time-dependent changes in lysosomal cholesterol content and lipid droplet formation. Our results indicate that the L472P change present in NPC1 WT-V compromises NPC1 functionality in lysosomal cholesterol export. All-atom molecular dynamics simulations suggest that the L472P change alters the relative position of the NPC1 middle and the C-terminal luminal domains, disrupting the recently characterized cholesterol efflux tunnel. These results reveal functional defects in NPC1 WT-V and highlight the strength of simulations and quantitative imaging upon stable protein expression in elucidating subtle differences in protein function.

KEYWORDS

cholesterol transport, gene variants, late endosomes, lipid droplets, lysosomal storage diseases, Niemann-Pick C1

1 | INTRODUCTION

Cholesterol is essential for normal cellular functions as it modulates the properties of cell membranes and affects the functions of membrane-associated proteins. Receptor-mediated endocytosis of low-density lipoproteins (LDL) brings exogenous cholesterol to the endosomal compartment where LDL particles dissociate and the released cholesterol esters are hydrolyzed by lysosomal acid lipase to produce free cholesterol.[1] Cholesterol is subsequently transported out of the endo-lysosomal compartment to other membranes, such as the plasma membrane and the endoplasmic reticulum (ER).[2] Cellular cholesterol levels are monitored in the ER by a delicate regulatory machinery that

responds to alterations in cholesterol levels by adjusting cellular cholesterol synthesis and cholesterol uptake accordingly.[3] Excess cholesterol in the ER is esterified by the ER membrane protein sterol O-acyltransferase (SOAT, a.k.a. ACAT) to generate cholesterol esters that are stored in lipid droplets for later use in lipid poor conditions.[4]

Niemann-Pick C1-protein (NPC1) plays a central role in the export of cholesterol from the endo-lysosomal system.[5,6] NPC1 is a glycoprotein with 13 transmembrane segments[7] and three large luminal domains, the N-terminal domain (NTD), the middle luminal domain (MLD), and the C-terminal luminal domain (CTD).[8,9] It locates in endo-lysosomal membranes, orchestrating cholesterol egress together with NPC2, a soluble lysosomal cholesterol-binding protein. According to the prevailing view, the MLD of NPC1 recruits NPC2 to deliver luminal cholesterol to the sterol binding NTD of NPC1.[6] Recent findings suggest the existence of an NPC1 intramolecular tunnel through which cholesterol passes the lysosomal glycocalyx prior to insertion to the lysosomal limiting membrane.[10]

Loss of function mutations in the NPC1 gene lead to the build-up of cholesterol in the endo-lysosomal compartment and a progressive neurodegenerative disorder, NPC disease, which leads to premature death.[11] Genetic testing together with staining of patient cells with filipin, a fluorescent cholesterol-binding compound, are used to confirm the disease diagnosis. There are over 300 described NPC disease-causing mutations spanning nearly the whole NPC1 protein.[12,13] A specific mutation may present with different phenotypes indicating that a particular mutation only partially contributes to the clinical disease manifestations. In addition, some genetic variants represent benign polymorphisms but NPC disease carriers and patients may also possess rare variants of unknown significance.

A cloned cDNA construct of NPC1, named NPC1 WT-V[14] that has been used as wild-type NPC1 in publications by us and others,[14-25] also contains four variants in comparison to the Genbank reference sequence.[26] These variants are 387 T>C (Y129Y), 1415 T>C (L472P), 1925 T>C (M642T) and 2587 T>C (S863P). Thus, three of them change the amino acid sequence, with L472P located in the MLD, M642T in the second cytoplasmic loop, and S863P in the CTD.

In this work, we established a system for detecting subtle functional effects of NPC1 variants by combining stable and moderate protein expression with high-content imaging and image analysis, using the NPC1 WT-V as a test case. Our data indicate that the L472P change affects the subcellular distribution of NPC1 and compromises the cholesterol export function of the protein. All-atom molecular dynamics (MD) simulations suggest that this mutation can disrupt the conformation of luminal domains and the cholesterol efflux tunnel of NPC1.

2 | RESULTS AND DISCUSSION

2.1 | Stable expression of NPC1 variants

To investigate the function of NPC1 variants, we first disrupted the endogenous NPC1 locus using CRISPR/Cas9-mediated editing in human A431 cells that are well suited for genetic engineering and imaging (Figure 1A). The generated NPC1-KO cells (Figure S1A,B) lacked immunoreactive NPC1 protein (Figure 1) and showed a strong punctate, perinuclear filipin staining, indicative of cholesterol accumulation in the late endosomal compartments (Figure 2A). NPC1 variant constructs containing a C-terminal EGFP fusion were subsequently inserted into the AAVS1 safe harbor site in the NPC1-KO cells. Stable

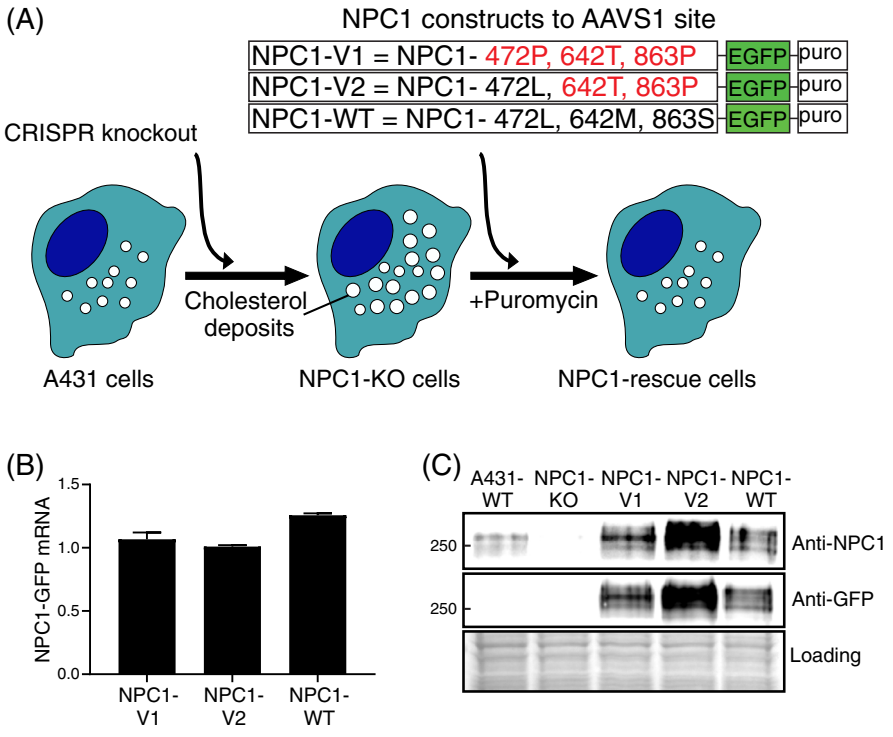

FIGURE 1 Stable expression of NPC1 variants. (A), Outline for the generation of stable cell lines. NPC1-KO A431 cells were generated by CRISPR/Cas9 technology. NPC1-V1, NPC1-V2, and NPC1-WT tagged with EGFP and puromycin selection marker were introduced into the AAVS1 safe harbor site of NPC1-KO cells to generate NPC1-rescue cells. Pools of NPC1-rescue cells were selected using puromycin. NPC1-WT = Genbank reference sequence. Amino acid changes in constructs NPC1-V1 and NPC1-V2 compared to the NPC1-WT construct are highlighted with red. (B), NPC1-GFP transcript levels in complete medium, triplicate determinations from pooled duplicate samples. Data are mean ± SEM. (C), NPC1 protein levels in A431-WT, NPC1-KO, NPC1-V1, NPC1-V2, and NPC1-WT cell pools

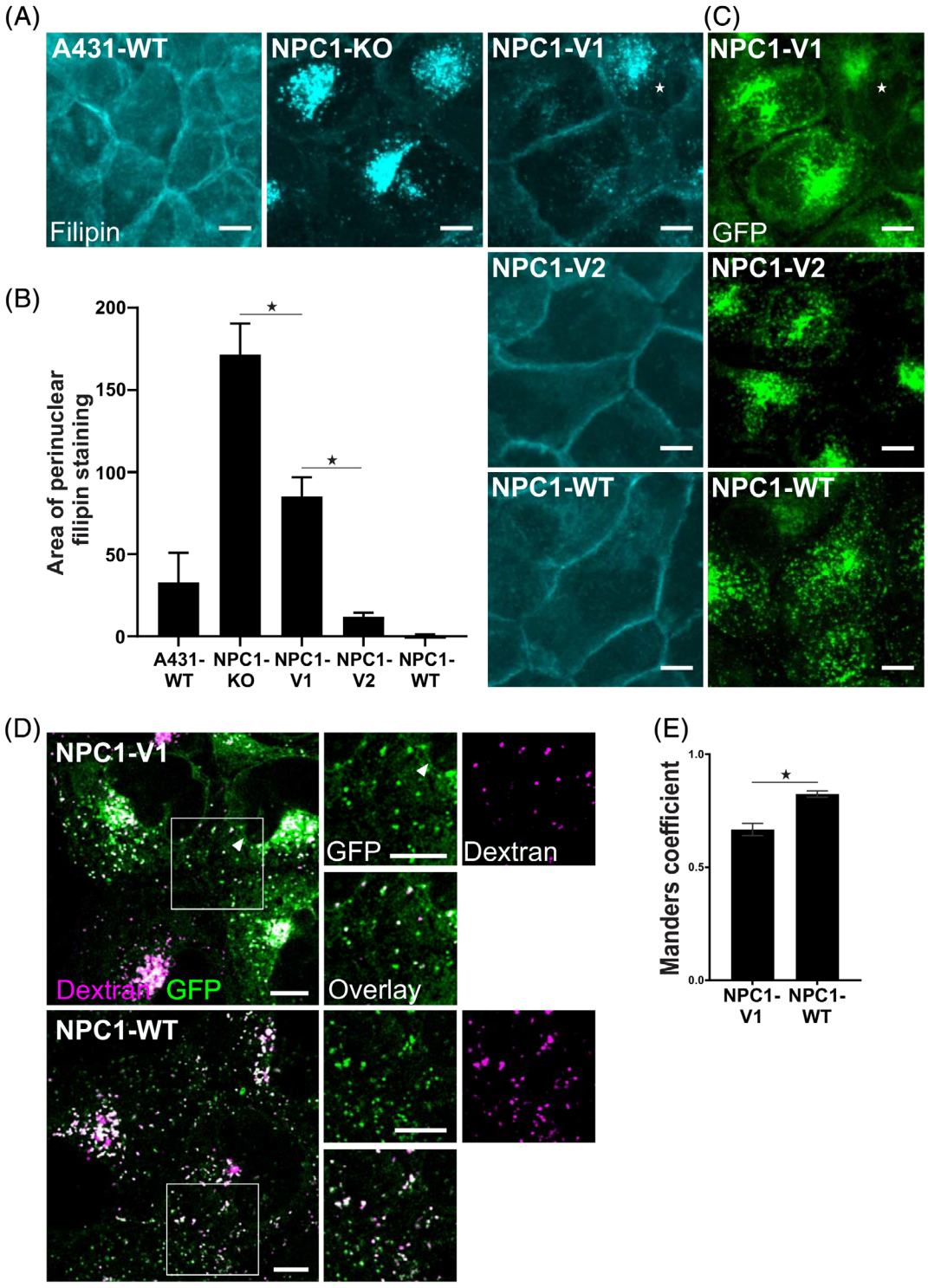

FIGURE 2 Localization of cholesterol and NPC1-GFP in the cell lines. (A), Widefield microscopy images of cells in complete medium, fixed, and stained with filipin. (B), Quantification of the pixel area of perinuclear filipin staining, mean ± SEM. For A431-WT, n = 20; NPC1-KO, n = 28; NPC1-V1, n = 32; NPC1-V2, n = 43, and NPC1-WT, n = 31 cells. *t*-test **P* < 0.001. (C), Widefield microscopy images of the same cells as in panel A, showing NPC1-GFP localization. * indicates a cell with residual filipin staining and partially mislocalized NPC1-V1-GFP. (D), Live confocal images of Dextran labeled cells expressing NPC1-V1-GFP or NPC1-WT-GFP in LPDS. Please note the reticular, ER-like appearance of NPC1-V1, as evidenced by the nuclear envelope labeling (white arrowhead). (E), Quantification of colocalization of GFP and Dextran, mean ± SEM. For NPC1-V1, n = 40 cells and for NPC1-WT, n = 44 cells. t-test **P* < 0,001. Scale bars 10 μm

cell pools expressing NPC1-GFP variants at moderate levels were selected using puromycin.

We focused on the functional differences between three NPC1 variant cell types, hereafter referred to as NPC1-V1, NPC1-V2, and NPC1-WT that were compared to A431 wild-type (WT, non-engineered) and NPC1-KO cells. NPC1-V1 has the aforementioned L472P, M642T and S863P changes in comparison to the Genbank reference sequence (here called NPC1-WT sequence). NPC1-V2 has the 642T and 863P changes but retains 472L (Figure 1A). All the NPC1 variants were expressed at similar mRNA levels (Figure 1B). NPC1-V1 and NPC1-WT cells moderately overexpressed NPC1 compared to the endogenous A431 NPC1 protein level, while NPC1-V2 showed higher expression (Figure 1C). The obvious cholesterol accumulation in NPC1-KO cells compared to A431-WT cells was reduced in the NPC1-overexpressing cells. However, NPC1-V2 and NPC1-WT appeared to revert the NPC1-KO phenotype more efficiently than NPC1-V1 (Figure 2A,B).

We next assessed the subcellular distribution of the NPC1 variants by imaging. NPC1-V2 and NPC1-WT cells displayed punctate structures colocalizing with the lysosomal tracer Dextran (Figure 2C-E). Instead, NPC1-V1 often displayed a reticular, ER-like pattern (Figure 2D) and less colocalization with Dextran, suggesting that NPC1-V1 is partly mislocalized (Figure 2C-E). NPC1-V1 mislocalization seemed to correlate with cholesterol accumulation, as cells with diffuse/reticular NPC1-V1-GFP pattern typically showed a stronger filipin staining than cells with more punctate NPC1-V1-GFP (Figure 2A,C).

2.2 | Cell treatments and high-content imaging

To assess the intracellular delivery of LDL-derived cholesterol, we performed lipid manipulations to challenge the cholesterol transport machinery in these cells. Cells were delipidated by a 24-hour treatment with 5% lipoprotein deficient serum (LPDS)-containing media to upregulate LDL-receptor expression (Figure S2). Thereafter, cells were loaded with 100 μg/mL of LDL for increasing times, fixed, and stained (Figure 3A). For assessment of free cholesterol in late endosomal compartments, cells were stained with filipin and anti-LAMP1 antibodies (Figure 3B). A plasma membrane marker (CellMask Green) and a nuclear marker (TO-PRO-3) were included to facilitate image analysis (Figure 3C). Cells were then imaged using an automatic microscope and the acquired images automatically segmented (Figure 3D), enabling the analysis of filipin intensity in LAMP1-positive organelles from hundreds of cells per condition. For the assessment of LDL-induced lipid droplet formation, cells were stained with the lipophilic dye LD540[27] and a nuclear marker (DAPI) (Figure 3E), and the cells were similarly automatically imaged and analyzed to quantify the number of lipid droplets (Figure 3F).

2.3 | LDL-induced increase in lysosomal cholesterol content

Filipin staining detected a reduction in lysosomal cholesterol content upon LPDS treatment (Figure S3A) and an increase upon LDL loading (Figure 4A-C). NPC1-KO cells showed a roughly 2-fold higher filipin intensity in LAMP1 organelles even in LPDS compared to A431-WT cells (Figure 4C). Moreover, NPC1-KO cells accumulated substantially more filipin in LAMP1 positive structures upon LDL loading compared to A431-WT cells (Figure 4C).

NPC1-V1 cells also showed cholesterol accumulation with respect to A431-WT cells, with a roughly 1.5-fold higher filipin intensity in LAMP1 positive structures after LPDS treatment (Figure 4C). Moreover, NPC1-V1 cells reached the level of late endosomal cholesterol accumulation in NPC1-KO cells in 4 hours of LDL loading and upon continued LDL loading, the filipin intensity increased similarly to NPC1-KO cells. NPC1-V2 and NPC1-WT cells had similar levels of cholesterol as A431-WT cells after LPDS treatment (Figure 4C). However, NPC1-WT and NPC1-V2 expressing cells did not appreciably accumulate cholesterol in the late endosomal organelles upon LDL loading (Figure 4C). This speaks for the idea that cholesterol egress from late endosomes is enhanced upon overexpression of a functional NPC1 protein. Together, these findings strongly suggest a defect in the cholesterol transporting capacity of NPC1-V1. This defect was not observed in NPC1-V2 cells, which acted similarly to NPC1-WT cells upon LDL-loading, implying that the L472P change affects NPC1 function.

2.4 | LDL-induced lipid droplet formation

A readout for LDL-cholesterol transport to the ER is the formation of lipid droplets. To assess cholesterol transport from the late endosomes/lysosomes to the ER in NPC1-variant-expressing cells, we counted their lipid droplets, marked by LD540, upon LDL loading (Figure 5A,B).

LPDS treatment diminished the cellular cholesterol storage pool, as indicated by very low lipid droplet counts (Figure S3B, Figure 5B). Upon LDL loading, NPC1-KO cells formed lipid droplets less avidly than A431-WT cells, in consistence with the reduced clearance of LDL-derived cholesterol from the endosomal compartments in the absence of functional NPC1. Lipid droplet formation clearly increased after 4 hours of LDL loading in A431-WT, NPC1-V2, and NPC1-WT cells and further increased thereafter. Instead, in NPC1-KO and NPC1-V1 cells lipid droplet formation was not clearly observed at 4 hours and showed a very mild increase thereafter. NPC1-V1 and NPC1-KO cells behaved essentially identically in this assay, further supporting the idea that the L472P change disrupts NPC1 function.

2.5 | The effects of the mutations on NPC1 structure

To investigate the effects of individual mutations on the NPC1 structure, we performed all-atom MD simulations of the membrane-embedded full-length NPC1 variants, that is, wild-type (NPC1-WT),

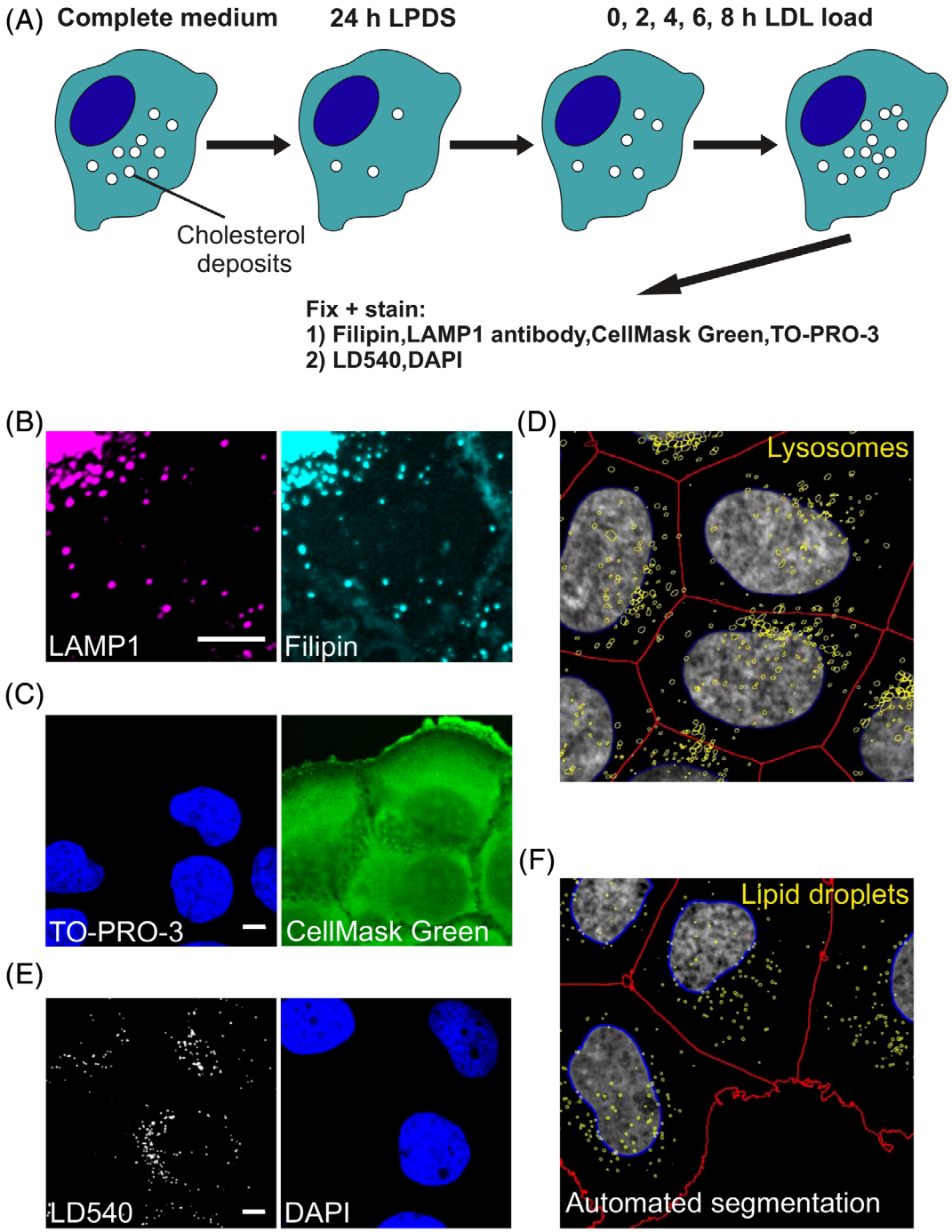

FIGURE 3 Cell treatments and high-content imaging. (A), Outline of cell treatments prior to imaging. Cells are seeded in 384-well high content imaging plates in 10% FBS-containing complete medium for 2 days, then treated with 5% LPDS for 24 hours, loaded with 100 μg/mL LDL for 0 to 8 hours, fixed with 4% PFA and stained with filipin, LAMP1 antibody, CellMask Green, and TO-PRO-3 to analyze free cholesterol in the late endosomal compartments, or with LD540 and DAPI to analyze the number of lipid droplets. (B), Exemplary images of LAMP1 and filipin stainings. (C), Exemplary images of nuclear (TO-PRO-3) and plasma membrane (CellMask Green) stainings. (D), Automatic cell segmentation and detection of LAMP1 positive organelles (yellow circles) in CellProfiler. (E), Exemplary images of LD540 stained lipid droplets and DAPI stained nuclei. (F), Automatic cell segmentation and detection of lipid droplets (yellow circles) in CellProfiler. Scale bars 10 μm

L472P, M642T, and S863P (see Figure 6A for a representation of NPC1 structure and the definition of the domains). All-atom MD simulations complement experiments by providing exceptional insight into the dynamics of protein-lipid complexes.[28,29] In the same spirit, we analyzed the effects of the mutations on the local and global conformation of NPC1 in comparison to the NPC1-WT.

In all NPC1 variants, the transmembrane domain of NPC1 was found to be stable and remain close to the initial conformation: the

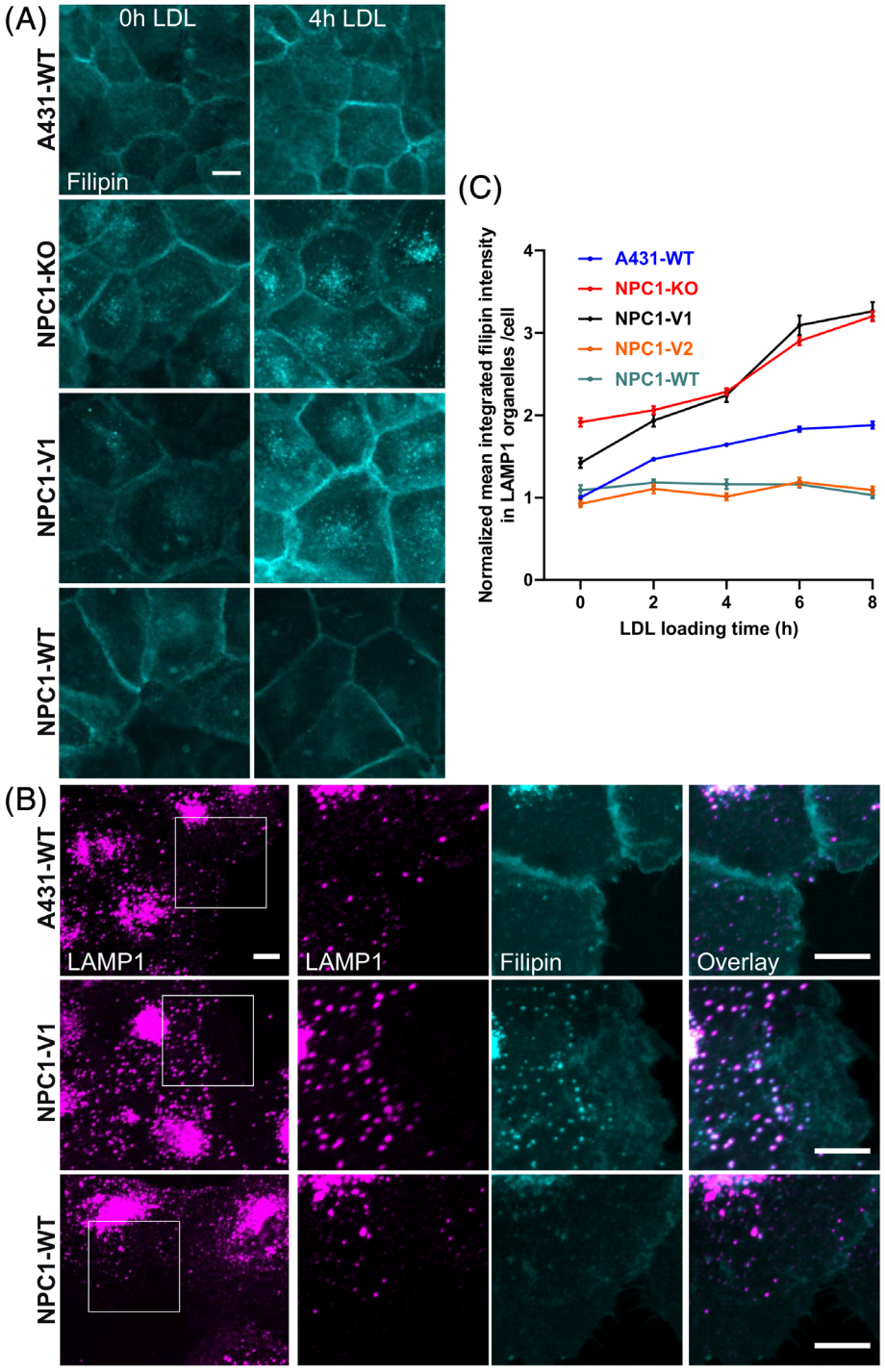

FIGURE 4 LDL-induced increase in lysosomal cholesterol content. (A), Widefield microscopy images of cells treated with LPDS for 24 hours (0 h LDL) and loaded with LDL for 4 hours, fixed, and stained with filipin. (B), Confocal images of free cholesterol and late endosomal organelles. A431-WT, NPC1-V1, and NPC1-WT cells were fixed and stained with filipin and LAMP1-antibody after 24 hours LPDS and 8 hours 100 μg/mL LDL treatment. (C), Quantification of LDL-induced changes in filipin intensity in LAMP1-organelles at 0 to 8 hours of LDL loading. For A431-WT, n = 1476 to 2457 cells and for NPC1-KO, n = 728 to 1032 cells from four independent experiments each with duplicate wells for each condition. For NPC1-V1, n = 326 to 646; NPC1-V2, n = 455 to 630, and NPC1-WT, n = 580 to 769 cells from two independent experiments each with duplicate wells per condition. The mean integrated filipin intensity in each detected LAMP1 organelle for each cell is measured. Each value is normalized to the corresponding value in A431-WT 0 hour LDL condition and normalized values are presented ± SEM. Scale bars 10 μm

root-mean-square deviation (RMSD) of the C_α and the heavy atoms of the transmembrane helices were below 2.0 and 2.3 Å with respect to the initial conformation, respectively. The luminal domains, however, manifested substantial conformational flexibility in all variants. This is demonstrated by maximum C_α RMSD values that were in the range of 3.3-4.8 Å for the MLD, and 3.1-3.9 Å for the CTD, indicating the conformational stability of these individual domains to be lower compared to the transmembrane domain.

Interestingly, we observed a large reorganization of the luminal domains in the L472P variant. The 472P mutation resulted in a clockwise rotation of the CTD with respect to the MLD, when viewed from the endosomal lumen (Figure 6B; compare bottom left with top left), and this configuration remained stable for the rest of the simulation. The observed large reorganization is likely to affect NPC1-V1 conformation and contribute to its impaired exit from the ER. Recent experimental evidence suggests that the interface between MLD and CTD features a cholesterol transport tunnel.[10] To evaluate the effect of the rotation of the luminal domains in the L472P variant, we analyzed the shape of the tunnel in the wild-type and the L472P variant (Figure 6B, right panels). While the wild-type conformation features a

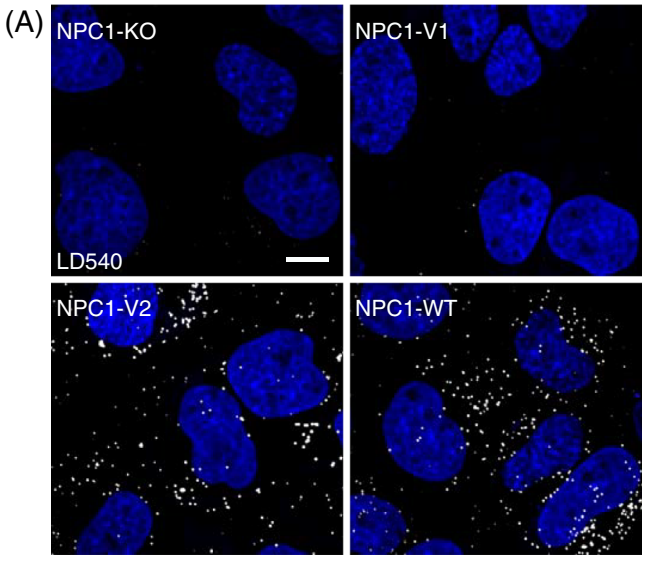

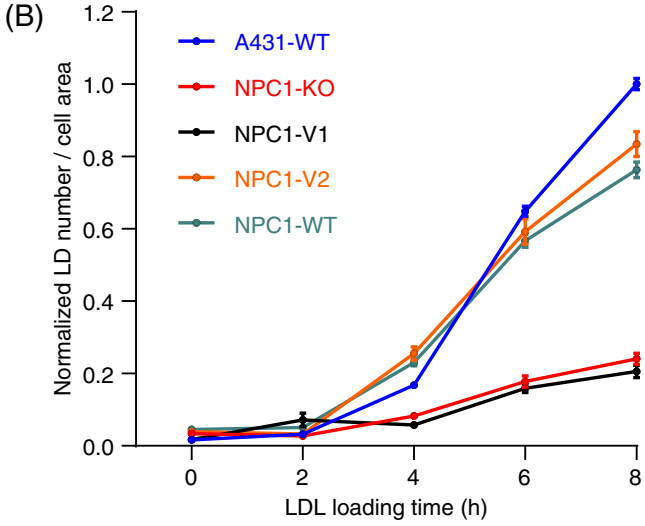

FIGURE 5 LDL-induced increase in lipid droplet formation. (A), Confocal images of lipid droplets. NPC1-KO, NPC1-V1, NPC1-V2, and NPC1-WT cells were fixed and stained with LD540 and DAPI after 24 hours LPDS and 8 hours 100 μg/mL LDL treatment. Scale bar 10 μm. (B), Quantification of LDL-induced changes in lipid droplet numbers at 0 to 8 hours LDL loading. For A431-WT, n = 1528 to 1832 cells and for NPC1-KO, n = 464 to 580 cells from four independent experiments each with duplicate wells per condition. For NPC1-V1, n = 104 to 528; NPC1-V2, n = 242 to 338, and NPC1-WT, n = 700 to 1038 cells from two independent experiments each with duplicate wells per condition. Lipid droplet number is normalized to the cell area and to the mean of A431-WT 8 hours LDL load condition. Mean of the normalized values presented ± SEM

putative cholesterol tunnel between the luminal domains (Figure 6B top right), the continuity of this tunnel is broken in the L472P variant (Figure 6B bottom right). This suggests that the conformational change in the L472P variant hinders cholesterol transport from the NTD to the membrane and functionally compromises NPC1-V1.

The M642T and S863P variants are accompanied with local conformational changes (Figure 6C,D, respectively) and can result in a rotation of the MLDs. On the other hand, the continuity of the cholesterol transport tunnel remains mostly intact in these variants. The M642T mutation also results in the extension of the cytoplasmic loop 2 toward the aqueous phase (Figure 6C). This is likely because the substitution of Met with Thr increases the hydrophilicity of this loop, which connects transmembrane helices 3 and 4. Figure 6C highlights the extensive contacts between the membrane lipids and the 642M residue. In contrast, 642T was positioned in the water phase and did not interact directly with the lipids. This increases the exposure of the neighboring 643K to the cytoplasmic milieu, possibly making it more prone to ubiquitylation, as previously suggested.[30] As ubiquitylation affects protein trafficking and stability, we speculate that this might be related to the higher protein expression of NPC1-V2 compared to NPC1-WT. On the other hand, the reason for the lower expression of NPC1-V1 that also possesses 642T might be its partial retention in the ER and faster turnover, as previously suggested for the NPC1 mutant I1061T.[31]

Our results provide evidence that the dissection of subtle changes in NPC1 function is facilitated by stable, moderate protein expression in combination with high-content imaging and analysis. This is evident for the 472P-variant, as NPC1-V1 is distributed differently and has impaired function when compared to NPC1-V2 and NPC1-WT, both harboring 472L. Indeed, in earlier studies typically based on transient, high protein overexpression and analysis of smaller cell numbers, NPC1-V1 has been considered to behave as a wild-type protein. Of note, a relatively large fraction of NPC1-V1 has been reported to be endoglycosidase H sensitive,[25] in line with a potential defect in its ER exit. In general, based on the above information, using NPC1-V1 as "WT" background dampens the conclusions when dissecting the effects of individual NPC1 sequence variants.

The all-atom simulations suggest that 472P changes NPC1 conformation. The conformational changes in the protein may contribute to the apparent defect in the ER export of NPC1-V1 and affect its postulated cholesterol transport tunnel. Remarkably, the clinical relevance of the L472P-change is supported by a recent report of two Iranian NPC1-patients carrying this mutation.[32] The high-content LDL-cholesterol transport assays based on quantitative monitoring of lysosomal and lipid droplet lipid accumulation described here, may prove useful in several settings. Besides discovering novel function-modulating variants of NPC1, they may be employed, for instance, to assess potential therapeutics for specific NPC-disease genotypes.

3 | MATERIALS AND METHODS

3.1 | Materials

Mouse anti-LAMP1 (DSHB, Cat# H4A3, RRID:AB_2296838, Immunofluorescence 1:400), Rabbit anti-NPC1 (Abcam, Cat# ab134113, RRID:AB_2734695, Immunoblot 1:2000), Mouse anti-GFP (Abcam, Cat# ab1218, RRID:AB_298911, Immunoblot 1:2000), Alexa 568 goat anti-mouse (Molecular probes, Cat# A-11004, RRID:AB_2534072, Immunofluorescence 1:500), Filipin (Sigma, F9765), CellMask Green

(Life Technologies/Thermo Fisher, H32714), TO-PRO-3 iodide (Thermo Fisher, T3605), DAPI (Sigma, D9542), LD540 (Princeton BioMolecular Research), Dextran Alexa-Fluor 647,10 000 MW (Molecular Probes [Invitrogen], D22914). Cell culture reagents and general reagents were purchased from GibCo/Thermo Fisher, Lonza, and Sigma-Aldrich. Lipoprotein-deficient serum (LPDS) was made from fetal bovine serum (FBS) as previously described.[33] LDL was prepared from pooled plasma of healthy donors by sequential ultracentrifugation as previously described.[33]

3.2 | DNA constructs

AAVS1 safe harbor locus site-specific integration was performed with CRISPR/Cas9-mediated HDR. The open reading frame of NPC1 was taken from pCR3.1[21] and EGFP was linked to the C-terminal of NPC1 and cloned into the safe harbor vector pSH-FIRE-P-AtAFB2 (Addgene, #129715) to obtain pSH-NPC1-V1-EGFP. This NPC1 vector contains three amino acid changing variants (L472P, M642T and S863P) as earlier reported.[14] pSH-NPC1-V2-EGFP was constructed by replacing the fragment containing L472P with the corresponding Genbank reference sequence devoid of this variant. pSH-NPC1-WT-EGFP is based on the Genbank reference sequence for NPC1, and the NPC1-WT-EGFP open reading frame was ordered from Genescript.

3.3 | Generation of cell lines

CRISPR/Cas9-mediated genome engineering was used to generate NPC1 A431 knockout cells (NPC1-KO). Briefly, sgRNA guides corresponding to the AATCCAGTTGGTGGCATTACAGG and GTTCAATAAGGACAATGGACAGG sites of NPC1 were synthesized and cloned into the sgRNA expression vector (pGL3-puro-sgRNA) using BbsI sites. A431 cells were co-transfected with a Cas9 nickase encoding plasmid (pcDNA4-Cas9nickase-2A-GFP) and the two sgRNA expressing plasmids using Lipofectamine LTX with Plus reagent (Invitrogen, Cat#15338100), after 24 hours cells were incubated with puromycin (1 μg/mL) for 48 hours.[34] Cells were further incubated in normal culture medium without puromycin for 4 days. Single clones were isolated and verified for cholesterol accumulation by filipin staining. Sequencing of the NPC1-KO clone (T1A) used in this study revealed two deletions in NPC1 exon 5 (Figure S1) and no NPC1-WT allele.

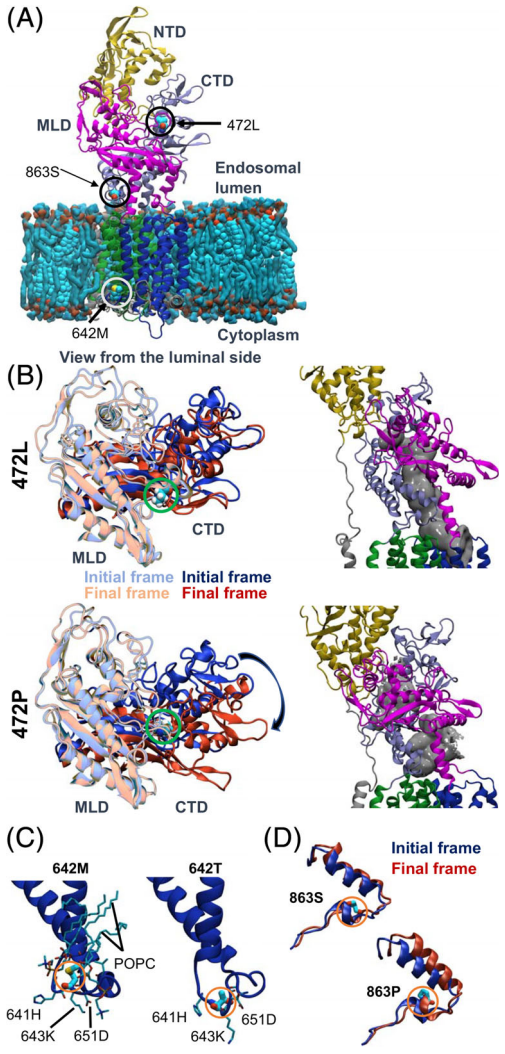

FIGURE 6 Legend on next column.

FIGURE 6 Effects of mutations on the conformation of NPC1. (A), A representative snapshot of the simulation system of the NPC1-WT. The protein is shown in cartoon representation with each domain colored and labeled differently: N-terminal domain (NTD; residues 23-261), middle luminal domain (MLD; residues 372-620), and C-terminal domain (CTD; residues 854-1097); additionally, the transmembrane domains are highlighted separately (residues 262-371, 621-783 in green and residues 784-853, 1098-1278 in blue). A slice of the membrane is shown with POPC in surface and cholesterol in van der Waals (VdW) representation. Water and ions are omitted for clarity. The residues that were mutated in this study are shown in VdW representation and circled. (B), L472P mutation results in a major rearrangement in the luminal domains. (left panels) The initial structure (blue for CTD and light blue for MLD) and the final structures (red for CTD and orange for MLD) from the wildtype (top panel) and the mutant (bottom panel) NPC1 simulations are shown in cartoon representation viewing from the luminal side. Only MLD and CTD structures are shown, and the C_α atoms of MLD are superposed to show the extent of the conformational change clearly. The arrow points the change of CTD position with respect to MLD. (right panels) The configurations of the cholesterol transport tunnel (shown in gray) for the NPC1-WT and L472P conformations are shown.(C), M642T results in a slight extension of the loop into the cytoplasmic side and loss of lipid contacts. The final conformations (only residues 620 to 680 are shown for clarity) from the wild type (left) and the mutant (right) NPC1 simulations are depicted. The protein and lipid residues within 3 Å of residue 642 are shown in licorice representation and labeled. (D), The local conformation in the S863P mutation. Residues 857 to 887 are shown in cartoon representation, and the rest of the protein is omitted for clarity. The initial (blue) and final (red) structures from the simulations are overlaid after superposing protein C_α atoms (wild type, top left; mutant, bottom right)

A431 NPC1 knockout cells were used to generate stable cell pools expressing NPC1-EGFP proteins. Briefly, pSH-NPC1-V1-EGFP, pSH-NPC1-V2-EGFP or pSH-NPC1-WT-EGFP were transfected with plasmid pCas9-sgAAVS1-2[35] (Addgene, #129727) for integration into the AAVS1 safe harbor locus[36] using the X-tremeGENE reagent HP DNA transfection reagent (Sigma), and the cells were grown in culture medium containing puromycin 1 μg/mL until a resistant cell pool was obtained.

3.4 | Cell culture and lipid manipulations

A431 cells (ATCC, Cat# CRL-1555, RRID:CVCL_0037) were maintained in Dulbecco's Modified Eagle's Medium (DMEM) with 10% fetal bovine serum (FBS), penicillin/streptomycin (100 U/mL each), and L-glutamine (2 mM) at 37°C in 5% CO_2. Generated NPC1-expressing cell lines were maintained in the presence of 1 μg/mL puromycin. All cell lines were regularly tested negative for mycoplasma infection by PCR. For imaging experiments, cells were plated on imaging plates (Corning) and delipidated by 24-hour treatment with serum-free medium supplemented with 5% LPDS. Following LPDS treatment cells were loaded with 100 μg/mL LDL in 5% LPDS for 0 to 8 hours.

3.5 | Cell stainings

For confocal and widefield imaging of fixed cells, cells were washed with PBS and fixed with 4% PFA in 250 mM Hepes, pH 7.4, 100 μM $CaCl_2$ and 100 μM $MgCl_2$ for 20 minutes. Subsequently, cells were washed with PBS, quenched in 50 mM NH_4Cl for 15 minutes and washed with PBS. Cells were stained and permeabilized with filipin (0.5 mg/mL) in PBS/10% FBS and washed with PBS. Subsequently, cells were incubated with primary antibody LAMP1 (1:400) in PBS/10%FBS for 45 minutes, washed with PBS before incubation with secondary antibody anti-mouse Alexa 568 (1:500), CellMask Green (1 μg/mL), and TO-PRO3 (0.5 μg/mL) in PBS/10%FBS for 45 minutes. To stain lipid droplets, cells were washed with PBS after fixation and incubated for 30 minutes with LD540 (1 μg/mL) and DAPI (5 μg/mL) in PBS. All stainings were done at room temperature. After staining, cells were washed with PBS and imaged in PBS. For filipin staining only, cells were grown on cover slips, washed with PBS after filipin permeabilization and mounted (ProLong Glass Mountant, ThermoFisher) on microscopy slides. For live confocal imaging (Figure 2D), cells were grown on a LabTek glass-bottom dish coated with fibronectin, treated with LPDS for 24 hours to decrease the perinuclear accumulation of late endocytic organelles, and stained with Dextran Alexa-Fluor 647 at 5 μg/mL for 3 hours. Cells were then washed with PBS and imaged in Gibco FluoroBrite DMEM with 5% LPDS.

3.6 | Imaging and image analysis

Cells were cultured on 384-well high content imaging plates (Corning) and imaged with PerkinElmer Opera Phenix automatic spinning-disk confocal microscope using a 63 x water objective, NA 1.15 or with a Nicon Eclipse Ti-E inverted widefield fluorescence microscope using a 40 x air objective, NA 0.75, and 1.5 x zoom. Z-stacks were acquired to span whole cells on filipin, LAMP1, CellMask, TOPRO-3, LD540, and DAPI channels. Widefield image stacks were automatically deconvolved using the Huygens batch processing application (https://svi.nl/HuygensSoftware). Image stacks were maximum intensity projected by custom MATLAB (http://www.mathworks.com/products/matlab/) scripts. LAMP1 organelles and lipid droplets were detected with CellProfiler.[37] Automatic cell segmentation and automatic image analysis were based on a previously described protocol.[38] Cells were segmented in a hierarchial manner starting with detection of cell nuclei in either TOPRO-3 or DAPI images based on the MoG adaptive and Otsu adaptive thresholding methods, respectively. Touching nuclei were separated by built-in intensity methods. Following nuclear detection, cytoplasm was detected in CellMask Green images or DAPI images using intensity propagation based on the Otsu global and Otsu adaptive thresholding methods, respectively, using the identified nuclei from the first step as a seed point. To detect lysosomes/late endosomes, LAMP1 images were thresholded using Otsu global method and lipid droplets were detected using a previously described CellProfiler module.[39] Integrated filipin intensity in each detected LAMP1-structure was measured and a mean value calculated per cell. All parameters were normalized to the mean of A431-WT 0 h LDL load condition. Lipid droplet counts were normalized to cell area, to exclude the effect of variation in cell size, and to the mean of A431-WT 8 h LDL load condition. Exemplary images' brightness and contrast are adjusted in ImageJ FIJI (http://fiji.sc) similarly in each figure except in Figure 2C (GFP) and 4B (LAMP1).

In Figure 2B, cellular cholesterol accumulation in complete medium was analyzed by quantifying the area of filipin signal after subtracting the cytoplasmic background and manually outlining the cells, leaving the plasma membrane outside the region of interest. In Figure 2D, cells were imaged live with Leica TCS SP8 X inverted confocal microscope using a 63 x water objective, NA 1.20, in an environmental chamber at 37°C, 5% CO_2. Images were deconvolved using HyVolution automated deconvolution. Cells were manually outlined and background was subtracted on Dextran and GFP channels. Colocalization of NPC1-GFP-positive organelles with Dextran-positive organelles was quantified using Manders colocalization coefficient in Fiji.

3.7 | Western blotting

Cells were lysed in buffer containing 1.0% Triton-X100, 20 mM Tris-HCl pH 7.5, 150 mM NaCl, and 1 mM EDTA with protease inhibitors. After 20 minutes incubation on ice, the lysate was centrifuged to get rid of nuclei. Equal amounts of the postnuclear lysates were loaded onto SDS-PAGE and transferred to nitrocellulose membrane (Protran, Whamann, PerkinElmerTM). The blots were incubated with appropriate antibodies. Goat-anti-mouse-HRP or goat anti-rabbit-HRP was used as secondary antibody. ECL was done according to the manufacturer's protocol (Bio-Rad). Images were acquired using the ChemiDocTM MP Imaging System (Bio-Rad).

3.8 | Quantitative reverse transcription PCR

Total RNAs were isolated using the NucleoSpin RNA isolation kit (Macherey-Nagel, Cat. 740955-250) and 1 μg of total RNA was transcribed using SuperScript VILO cDNA synthesis kit (Invitrogen). Quantitative reverse transcription-PCR was performed using Light Cycler 480 SYBR Green I Master Mix (Roche) and a Light Cycler 480 II (Roche). Reaction steps: 95°C for 5 minutes and 40 cycles of 95°C 10 seconds, 64°C 15 seconds, and 72°C 20 seconds. Relative quantities of mRNAs were normalized to 18S. Primers for PCR amplification were designed to span the NPC1-GFP-fusion site: AGGAACAGAGCGCGAACGGCTTC (forward) and GCTGAACTTGT GGCCGTTTACGT (reverse). Samples from A431-WT and NPC1-KO cells produced no NPC1-GFP signal. Primers for 18S: GTCTTGTAGTTGCCGTCGTCCTTG (forward) and GTCTTGTAG TTGCCGTCGTCCTTG (reverse), and for LDL receptor (Figure S2): TGGCTGCGTTAATGTGACACTC (forward) and AGCCGATCTTA AGGTCATTGC (reverse).

3.9 | Biomolecular simulations

3.9.1 | Model Preparation

The model for the full-length wild type NPC1 was constructed using RosettaCM[40] for cryo-EM density guided comparative modeling.[41] The crystal structure of the NTD (PDBID: 3GKH[6]) and that of the transmembrane and luminal domains (PDBID: 5 U74[42]) were used as templates. The initial model for the backbone of transmembrane helix 1 was adopted from the cryo-EM structure (PDBID: 3JD8[8]). Rigid body docking of the templates into the density[8] was performed using Chimera.[43] RosettaCM[40] was then used for the density-guided combination of the templates and modeling of the missing residues. One thousand models were generated, and the best scoring model that did not contain structural defects was subjected to a density-guided fast relax protocol of Rosetta. The intrinsic pK_a of the protein residues were determined using PROPKA 3.1[44] on the selected model. The protonation state of each residue was assigned based on the pK_a estimations and visual inspection considering the residue's position (pH~5 for luminal and pH~7 for transmembrane and cytoplasmic residues). VMD[45] psfgen plugin was used for building the all-hydrogen model for the wild type NPC1, and to model post-translational modifications and the point mutations: L472P, M642T and S863P. The topology format conversion to GROMACS was performed using the VMD TopoTools plugin.[46]

3.9.2 | Simulation systems

Each of the four variants was independently embedded in a hexagonal bilayer containing 260 POPC and 140 cholesterol molecules with random lateral distribution (35 mol% cholesterol) using in-house scripts. Each system was then solvated and neutralized with 0.15 M NaCl solution (62 000 water molecules, 167 Na^+, and 167 Cl^- ions). Next, the systems were independently subjected to a staged minimization and equilibration protocol using GROMACS 2016.x.[47] The heavy atoms of the protein and the head groups of the lipids were initially restrained (total of ~7 ns). The integration time step was ramped up from 1 to 2 fs and the restraints were released gradually during this protocol. The systems were heated to 310 K and pressurized at 1 atm using the Berendsen thermostat and barostat.[48] The final equilibrated configurations were used to start the production simulations.

3.9.3 | Simulation Protocols

All simulations were carried out using GROMACS 2016.x.[47] The protein and lipids were described using the Charmm36m[49] and Charmm36[50] force fields, respectively. TIP3P[51] water model and ion parameter set[52] distributed with the forcefield were used. The equations of motion were integrated using a leap-frog algorithm with a 2-fs time step. All bonds between hydrogen and heavy atoms were constrained using the LINCS algorithm.[53] Periodic boundary conditions were used along all three dimensions. For electrostatic interactions, a real space cut-off of 1.2 nm was used. Long-range electrostatic interactions were computed using the fast smooth Particle-Mesh Ewald (SPME) method with a Fourier spacing of 0.12 nm and a fourth-order interpolation. For the van der Waals interactions, a Lennard-Jones potential with a force-switch between 1.0 and 1.2 nm was used. All production simulations were performed in the *NpT* ensemble. The temperature was maintained at 310 K using the Nosé-Hoover thermostat.[54,55] Protein, membrane, and the solvent (water and NaCl) were coupled to separate temperature baths with a time constant of 1.0 ps. Semi-isotropic pressure coupling at 1 atm was performed using the Parrinello-Rahman barostat[56,57] with a time constant of 5 ps and a compressibility value of 4.5×10^{-5} bar^{-1}.

The NPC1-WT system was simulated for 2.5 μs and the mutant NPC1 systems for about 500 to 700 ns. Another shorter repeat (~300-400 ns) was performed for each mutant starting from the final configuration of the NPC1-WT system.

3.9.4 | Analyses

All analyses (RMSD, distances, etc.) were performed using tools distributed with GROMACS 2016[47] and VMD.[45] The analysis of the cholesterol efflux tunnels was performed using the HOLE program.[58] All molecular images were generated using VMD.[45]

ACKNOWLEDGMENTS

We thank Anna Uro for excellent technical support and Shiqian Li and Andrea Dichlberger for generating the NPC1 CRISPR knockout cell line. We acknowledge HiLIFE Light Microscopy Platform and Biocenter Finland for imaging resources and CSC—IT Center for Science Ltd for computing resources. This study was financially supported by the Academy of Finland (grant 307415 to E.I. and I.V.;

282192 and 312491 to E.I.), Sigrid Juselius Foundation (E.I., I.V.), HiLIFE (E.I., I.V.), and Orion Research Foundation (L.V.).

ORCID

Lauri Vanharanta https://orcid.org/0000-0002-7902-0009

REFERENCES

1. Ikonen E. Cellular cholesterol trafficking and compartmentalization. *Nat Rev Mol Cell Biol*. 2008;9(2):125-138. https://doi.org/10.1038/nrm2336.
2. Ikonen E. Mechanisms of cellular cholesterol compartmentalization: recent insights. *Curr Opin Cell Biol*. 2018;53:77-83. https://doi.org/10.1016/j.ceb.2018.06.002.
3. Goldstein JL, DeBose-Boyd RA, Brown MS. Protein sensors for membrane sterols. *Cell*. 2006;124(1):35-46. https://doi.org/10.1016/j.cell.2005.12.022.
4. Chang T-Y, Chang CCY, Ohgami N, Yamauchi Y. Cholesterol sensing, trafficking, and esterification. *Annu Rev Cell Dev Biol*. 2006;22(1):129-157. https://doi.org/10.1146/annurev.cellbio.22.010305.104656.
5. Carstea ED, Morris JA, Coleman KG, et al. Niemann-Pick C1 disease gene: homology to mediators of cholesterol homeostasis. *Science*. 1997;277(5323):228-231. https://doi.org/10.1126/science.277.5323.228.
6. Kwon HJ, Abi-Mosleh L, Wang ML, et al. Structure of N-terminal domain of NPC1 reveals distinct subdomains for binding and transfer of cholesterol. *Cell*. 2009;137(7):1213-1224. https://doi.org/10.1016/j.cell.2009.03.049.
7. Davies JP, Ioannou YA. Topological analysis of Niemann-Pick C1 protein reveals that the membrane orientation of the putative sterol-sensing domain is identical to those of 3-hydroxy-3-methylglutaryl-CoA reductase and sterol regulatory element binding protein cleavage-activating protein. *J Biol Chem*. 2000;275(32):24367-24374. https://doi.org/10.1074/jbc.M002184200.
8. Gong X, Qian H, Zhou X, et al. Structural insights into the Niemann-Pick C1 (NPC1)-mediated cholesterol transfer and ebola infection. *Cell*. 2016;165(6):1467-1478. https://doi.org/10.1016/j.cell.2016.05.022.
9. Li X, Wang J, Coutavas E, Shi H, Hao Q, Blobel G. Structure of human Niemann-Pick C1 protein. *Proc Natl Acad Sci U S A*. 2016;113(29):8212-8217. https://doi.org/10.1073/pnas.1607795113.
10. Winkler MBL, Kidmose RT, Szomek M, et al. Structural insight into eukaryotic sterol transport through Niemann-Pick type C proteins. *Cell*. 2019;179(2):485-497.e18. https://doi.org/10.1016/j.cell.2019.08.038.
11. Vanier MT. Complex lipid trafficking in Niemann-pick disease type C. *J Inherit Metab Dis*. 2014;38(1):187-199. https://doi.org/10.1007/s10545-014-9794-4.
12. NPC-db2: Niemann-Pick Type C Database. https://medgen.medizin.uni-tuebingen.de/NPC-db2/index.php. Accessed November 29, 2019.
13. The Human Gene Mutation Database. http://www.hgmd.cf.ac.uk/ac/gene.php?gene=NPC1. Accessed November 29, 2019.
14. Pipalia NH, Subramanian K, Mao S, et al. Histone deacetylase inhibitors correct the cholesterol storage defect in most Niemann-Pick C1 mutant cells. *J Lipid Res*. 2017;58(4):695-708. https://doi.org/10.1194/jlr.M072140.
15. Watari H, Blanchette-Mackie EJ, Dwyer NK, et al. Mutations in the leucine zipper motif and sterol-sensing domain inactivate the Niemann-Pick C1 glycoprotein. *J Biol Chem*. 1999;274(31):21861-21866. https://doi.org/10.1074/jbc.274.31.21861.
16. Watari H, Blanchette-Mackie EJ, Dwyer NK, et al. Niemann-pick C1 protein: obligatory roles for N-terminal domains and lysosomal targeting in cholesterol mobilization. *Proc Natl Acad Sci U S A*. 1999;96(3):805-810. https://doi.org/10.1073/pnas.96.3.805.
17. Millard EE, Srivastava K, Traub LM, Schaffer JE, Ory DS. Niemann-Pick type C1 (NPC1) overexpression alters cellular cholesterol homeostasis. *J Biol Chem*. 2000;275(49):38445-38451. https://doi.org/10.1074/jbc.M003180200.
18. Zhang M, Dwyer NK, Love DC, et al. Cessation of rapid late endosomal tubulovesicular trafficking in Niemann-Pick type c1 disease. *Proc Natl Acad Sci U S A*. 2001;98(8):4466-4471. https://doi.org/10.1073/pnas.081070898.
19. Pipalia NH, Cosner CC, Huang A, et al. Histone deacetylase inhibitor treatment dramatically reduces cholesterol accumulation in Niemann-Pick type C1 mutant human fibroblasts. *Proc Natl Acad Sci U S A*. 2011;108(14):5620-5625. https://doi.org/10.1073/pnas.1014890108.
20. Nakasone N, Nakamura YS, Higaki K, Oumi N, Ohno K, Ninomiya H. Endoplasmic reticulum-associated degradation of Niemann-Pick C1: evidence for the role of heat shock proteins and identification of lysine residues that accept ubiquitin. *J Biol Chem*. 2014;289(28):19714-19725. https://doi.org/10.1074/jbc.M114.549915.
21. Lusa S, Blom TS, Eskelinen EL, et al. Depletion of rafts in late endocytic membranes is controlled by NPC1-dependent recycling of cholesterol to the plasma membrane. *J Cell Sci*. 2001;114(10):1893-1900.
22. Blom TS, Linder MD, Snow K, et al. Defective endocytic trafficking of NPC1 and NPC2 underlying infantile Niemann-Pick type C disease. *Hum Mol Genet*. 2003;12(3):257-272. https://doi.org/10.1093/hmg/ddg025.
23. Wang C, Scott SM, Sun S, et al. Individualized management of genetic diversity in Niemann-Pick C1 through modulation of the Hsp70 chaperone system. *Hum Mol Genet*. 2020;29(1):1-19. https://doi.org/10.1093/hmg/ddz215.
24. Wang C, Scott SM, Subramanian K, et al. Quantitating the epigenetic transformation contributing to cholesterol homeostasis using Gaussian process. *Nat Commun*. 2019;10(1):5052. https://doi.org/10.1038/s41467-019-12969-x.
25. Roth DM, Hutt DM, Tong J, et al. Modulation of the maladaptive stress response to manage diseases of protein folding. *PLoS Biol*. 2014;12(11):12-14. https://doi.org/10.1371/journal.pbio.1001998.
26. NCBI GenBank reference sequence: NM_000271.4. https://www.ncbi.nlm.nih.gov/nuccore/NM_000271.4. Accessed October 21, 2019.
27. Spandl J, White DJ, Peychl J, Thiele C. Live cell multicolor imaging of lipid droplets with a new dye, LD540. *Traffic*. 2009;10(11):1579-1584. https://doi.org/10.1111/j.1600-0854.2009.00980.x.
28. Enkavi G, Javanainen M, Kulig W, Róg T, Vattulainen I. Multiscale simulations of biological membranes: the challenge to understand biological phenomena in a living substance. *Chem Rev*. 2019;119(9):5607-5774. https://doi.org/10.1021/acs.chemrev.8b00538.
29. Hollingsworth SA, Dror RO. Molecular dynamics simulation for all. *Neuron*. 2018;99(6):1129-1143. https://doi.org/10.1016/j.neuron.2018.08.011.
30. Scott C, Higgins ME, Davies JP, Ioannou YA. Targeting of NPC1 to late endosomes involves multiple signals, including one residing within the putative sterol-sensing domain. *J Biol Chem*. 2004;279(46):48214-48233. https://doi.org/10.1074/jbc.M406090200.
31. Gelsthorpe ME, Baumann N, Millard E, et al. Niemann-Pick type C1 I1061T mutant encodes a functional protein that is selected for endoplasmic reticulum-associated degradation due to protein misfolding. *J Biol Chem*. 2008;283(13):8229-8236. https://doi.org/10.1074/jbc.M708735200.
32. Hashemian S, Eshraghi P, Dilaver N, et al. Niemann-pick diseases: the largest Iranian cohort with genetic analysis. *Iran J Child Neurol*. 2019;13(2):155-162. https://doi.org/10.22037/ijcn.v13i2.20148.

33. Goldstein JL, Basu SK, Brown MS. Receptor-mediated endocytosis of low-density lipoprotein in cultured cells. *Methods Enzymol*. 1983;98(C):241-260. https://doi.org/10.1016/0076-6879(83)98152-1.
34. Salo VT, Belevich I, Li S, et al. Seipin regulates ER – lipid droplet contacts and cargo delivery. *EMBO J*. 2016;35(24):2699-2716. https://doi.org/10.15252/embj.201695170.
35. Li S, Prasanna X, Salo VT, Vattulainen I, Ikonen E. An efficient auxin-inducible degron system with low basal degradation in human cells. *Nat Methods*. 2019;16(9):866-869. https://doi.org/10.1038/s41592-019-0512-x.
36. Lombardo A, Cesana D, Genovese P, et al. Site-specific integration and tailoring of cassette design for sustainable gene transfer. *Nat Methods*. 2011;8(10):861-869. https://doi.org/10.1038/nmeth.1674.
37. Carpenter AE, Jones TR, Lamprecht MR, et al. CellProfiler: image analysis software for identifying and quantifying cell phenotypes. *Genome Biol*. 2006;7(10):100-110. https://doi.org/10.1186/gb-2006-7-10-r100.
38. Pfisterer SG, Gateva G, Horvath P, et al. Role for formin-like 1-dependent acto-myosin assembly in lipid droplet dynamics and lipid storage. *Nat Commun*. 2017;8:14858. https://doi.org/10.1038/ncomms14858.
39. Salo VT, Li S, Vihinen H, et al. Seipin facilitates triglyceride flow to lipid droplet and counteracts droplet ripening via endoplasmic reticulum contact. *Dev Cell*. 2019;50(4):478-493.e9. https://doi.org/10.1016/j.devcel.2019.05.016.
40. Song Y, Dimaio F, Wang RYR, et al. High-resolution comparative modeling with RosettaCM. *Structure*. 2013;21(10):1735-1742. https://doi.org/10.1016/j.str.2013.08.005.
41. DiMaio F, Tyka MD, Baker ML, Chiu W, Baker D. Refinement of protein structures into low-resolution density maps using Rosetta. *J Mol Biol*. 2009;392(1):181-190. https://doi.org/10.1016/j.jmb.2009.07.008.
42. Li X, Lu F, Trinh MN, et al. 3.3 Å structure of Niemann–Pick C1 protein reveals insights into the function of the C-terminal luminal domain in cholesterol transport. *Proc Natl Acad Sci USA*. 2017;114(34):9116-9121. https://doi.org/10.1073/pnas.1711716114.
43. Pettersen EF, Goddard TD, Huang CC, et al. UCSF chimera – a visualization system for exploratory research and analysis. *J Comput Chem*. 2004;25(13):1605-1612. https://doi.org/10.1002/jcc.20084.
44. Olsson MHM, SØndergaard CR, Rostkowski M, Jensen JH. PROPKA3: consistent treatment of internal and surface residues in empirical p K a predictions. *J Chem Theory Comput*. 2011;7(2):525-537. https://doi.org/10.1021/ct100578z.
45. Humphrey W, Dalke A, Schulten K. VMD: visual molecular dynamics. *J Mol Graph*. 1996;14(1):33-38. https://doi.org/10.1016/0263-7855(96)00018-5.
46. Vermaas JV, Hardy DJ, Stone JE, Tajkhorshid E, Kohlmeyer A. TopoGromacs: automated topology conversion from CHARMM to GROMACS within VMD. *J Chem Inf Model*. 2016;56(6):1112-1116. https://doi.org/10.1021/acs.jcim.6b00103.
47. Abraham MJ, Murtola T, Schulz R, et al. Gromacs: high performance molecular simulations through multi-level parallelism from laptops to supercomputers. *SoftwareX*. 2015;1-2:19-25. https://doi.org/10.1016/j.softx.2015.06.001.
48. Berendsen HJC, Postma JPM, Van Gunsteren WF, Dinola A, Haak JR. Molecular dynamics with coupling to an external bath. *J Chem Phys*. 1984;81(8):3684-3690. https://doi.org/10.1063/1.448118.
49. Huang J, Rauscher S, Nawrocki G, et al. CHARMM36m: an improved force field for folded and intrinsically disordered proteins. *Nat Methods*. 2016;14(1):71-73. https://doi.org/10.1038/nmeth.4067.
50. Klauda JB, Venable RM, Freites JA, et al. Update of the CHARMM all-atom additive force field for lipids: validation on six lipid types. *J Phys Chem B*. 2010;114(23):7830-7843. https://doi.org/10.1021/jp101759q.
51. Jorgensen WL, Chandrasekhar J, Madura JD, Impey RW, Klein ML. Comparison of simple potential functions for simulating liquid water. *J Chem Phys*. 1983;79(2):926-935. https://doi.org/10.1063/1.445869.
52. Beglov D, Roux B. Finite representation of an infinite bulk system: solvent boundary potential for computer simulations. *J Chem Phys*. 1994;100(12):9050-9063. https://doi.org/10.1063/1.466711.
53. Hess B, Bekker H, Berendsen HJC, Fraaije JGEM. LINCS: a linear constraint solver for molecular simulations. *J Comput Chem*. 1997;18(12):1463-1472. https://doi.org/10.1002/(SICI)1096-987X(199709)18:12<1463::AID-JCC4>3.0.CO;2-H.
54. Nosé S. A molecular dynamics method for simulations in the canonical ensemble. *Mol Phys*. 1984;52(2):255-268. https://doi.org/10.1080/00268978400101201.
55. Hoover WG. Canonical dynamics: equilibrium phase-space distributions. *Phys Rev A*. 1985;31(3):1695-1697. https://doi.org/10.1103/PhysRevA.31.1695.
56. Parrinello M, Rahman A. Polymorphic transitions in single crystals: a new molecular dynamics method. *J Appl Phys*. 1981;52(12):7182-7190. https://doi.org/10.1063/1.328693.
57. Nosé S, Klein ML. Constant pressure molecular dynamics for molecular systems. *Mol Phys*. 1983;50(5):1055-1076. https://doi.org/10.1080/00268978300102851.
58. Smart OS, Neduvelil JG, Wang X, Wallace BA, Sansom MSP. HOLE: a program for the analysis of the pore dimensions of ion channel structural models. *J Mol Graph*. 1996;14(6):354-360. https://doi.org/10.1016/S0263-7855(97)00009-X.

SUPPORTING INFORMATION

Additional supporting information may be found online in the Supporting Information section at the end of this article.

How to cite this article: Vanharanta L, Peränen J, Pfisterer SG, Enkavi G, Vattulainen I, Ikonen E. High-content imaging and structure-based predictions reveal functional differences between Niemann-Pick C1 variants. *Traffic*. 2020;1–12. https://doi.org/10.1111/tra.12727